PAPER

Fast ion transport during applied 3D magnetic perturbations on DIII-D

To cite this article: M.A. Van Zeeland *et al* 2015 *Nucl. Fusion* **55** 073028

View the article online for updates and enhancements.

Fast ion transport during applied 3D magnetic perturbations on DIII-D

M.A. Van Zeeland[1], N.M. Ferraro[1], B.A. Grierson[2], W.W. Heidbrink[2], G.J. Kramer[2], C.J. Lasnier[4], D.C. Pace[1], S.L. Allen[4], X. Chen[1], T.E. Evans[1], M. García-Muñoz[5], J.M. Hanson[6], M.J. Lanctot[1], L.L. Lao[1], W.H. Meyer[4], R.A. Moyer[7], R. Nazikian[2], D.M. Orlov[7], C. Paz-Soldan[1] and A. Wingen[8]

[1] General Atomics, PO Box 85608 San Diego, California 92186-5608, USA
[2] Princeton Plasma Physics Laboratory, PO Box 451, Princeton, NJ 08543-0451, USA
[3] University of California at Irvine, Irvine, California 92697, USA
[4] Lawrence Livermore National Laboratory, 7000 East Ave, Livermore, California 94550, USA
[5] Max-Planck-Institut fur Plasmaphysik, Euratom Association, Garching, Germany.
[6] Columbia University, New York, New York 10027, USA
[7] University of California San Diego, 9500 Gilman Dr., La Jolla, California 92093-0417, USA
[8] Oak Ridge National Laboratory, PO Box Oak Ridge, Tennessee 37831, USA

E-mail: vanzeeland@fusion.gat.com

CrossMark

Abstract

Measurements show fast ion losses correlated with applied three-dimensional (3D) fields in a variety of plasmas ranging from L-mode to resonant magnetic perturbation (RMP) edge localized mode (ELM) suppressed H-mode discharges. In DIII-D L-mode discharges with a slowly rotating $n = 2$ magnetic perturbation, scintillator detector loss signals synchronized with the applied fields are observed to decay within one poloidal transit time after beam turn-off indicating they arise predominantly from prompt loss orbits. Full orbit following using M3D-C1 calculations of the perturbed fields and kinetic profiles reproduce many features of the measured losses and points to the importance of the applied 3D field phase with respect to the beam injection location in determining the overall impact on prompt beam ion loss. Modeling of these results includes a self-consistent calculation of the 3D perturbed beam ion birth profiles and scrape-off-layer ionization, a factor found to be essential to reproducing the experimental measurements. Extension of the simulations to full slowing down timescales, including fueling and the effects of drag and pitch angle scattering, show the applied $n = 3$ RMPs in ELM suppressed H-mode plasmas can induce a significant loss of energetic particles from the core. With the applied $n = 3$ fields, up to 8.4% of the injected beam power is predicted to be lost, compared to 2.7% with axisymmetric fields only. These fast ions, originating from minor radii $\rho > 0.7$, are predicted to be primarily passing particles lost to the divertor region, consistent with wide field-of-view infrared periscope measurements of wall heating in $n = 3$ RMP ELM suppressed plasmas. Edge fast ion D_α (FIDA) measurements also confirm a large change in edge fast ion profile due to the $n = 3$ fields, where the effect was isolated by using short 50 ms RMP-off periods during which ELM suppression was maintained yet the fast ion profile was allowed to recover. The role of resonances between fast ion drift motion and the applied 3D fields in the context of selectively targeting regions of fast ion phase space is also discussed.

Keywords: fast ion transport, 3D magnetic perturbations, prompt beam loss, DIII-D tokamak

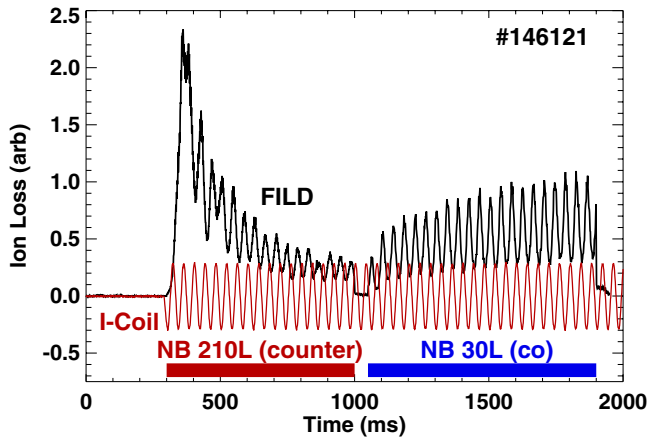(Some figures may appear in colour only in the online journal)

Figure 1. Midplane FILD signal showing modulation of fast ion loss correlated with rotating $n = 2$ field in DIII-D discharge 146121. In this and following figures, (co) and (counter) refer to beam injection in the direction of the plasma current and against the plasma current respectively.

1. Introduction

The adequate confinement of energetic particles (EPs), whether from injected heating beams, fusion reactions, or RF acceleration, is an essential requirement for future fusion devices. These fast ions play important roles in heating, momentum input, current drive and plasma stability yet are subject to transport from a variety of non-axisymmetric fields both static and time varying. Non-axisymmetric fields can come from any number of sources, including fields either intrinsic to a given device (error fields or ripple), MHD induced, or imposed by external coil systems [1–4]. This work focuses on the low toroidal mode number ($n = 2 - 3$) helical magnetic perturbations typically used for such things as edge-localized mode (ELM) control. Similar coils have been predicted to cause 5% or more loss of neutral beam ions in ITER plasmas [5–10], making the accurate and validated modeling of this interaction a priority. Of course, understanding how well fast ions are confined and where they go if lost due to externally applied 3D fields is a key part of not only predicting the performance and ensuring safe operation of future devices, but key for understanding, interpreting, and optimizing experiments on current devices.

The DIII-D tokamak is equipped with a set of six internal coils (I-coils) above and below the plasma midplane that are spaced uniformly in the toroidal direction and designed to make a radial field perturbation of up to ~120 G at the coil location immediately behind the first wall. These coils combined with two energy and pitch resolving fast ion loss detectors (FILDs) [11–13], an array of fast ion D_α (FIDA) [14] views spaced across the plasma midplane, and wide field-of-view infrared imaging system are utilized to investigate the impact of 3D fields on the fast ion population. An example measurement (which will be discussed further in section 3) showing fast ion loss clearly correlated with an applied $n = 2$ field is shown in figure 1.

In this paper, we first discuss our modeling approach employed to address the issue of fast ion loss associated with 3D fields then move on to discuss two quite different plasma regimes and the experimental data showing fast ion loss in each regime along with comparisons to modeling for each case. The first experimental regime presented is a DIII-D low-current, low beam power L-mode plasma in which the primary 3D field induced fast ion loss observed is a modulation of prompt beam ion loss. Following this, fast ion loss due to $n = 3$ resonant magnetic perturbation (RMP) fields in an ELM suppressed H-mode plasma is discussed. In both cases, many important features of the measured transport are captured by modeling giving confidence in our ability to predict this important effect in DIII-D and future devices. Finally, a potentially positive aspect of applied 3D fields is discussed where it is pointed out that resonances between fast ion orbits and the applied fields exist in these discharges and could be used to selectively target specific regions of fast ion phase space, something which will be the subject of future experimental work.

2. Modeling approach

The simulations presented in this paper combine full-orbit and beam deposition modeling with M3D-C1 [15–17] linear, two-fluid resistive MHD calculations of the plasma response to non-axisymmetric magnetic field perturbations. The validity of the linear response model may be estimated using an 'overlap criterion' that is described in [18]. In that reference, it was shown that internal measurements of the response were found to be in quantitative agreement with the linear response predictions even when the overlap criterion significantly exceeded unity. In the calculations presented here, the overlap criterion is less than unity throughout the plasmas, except in the steepest gradient region of the H-mode plasmas in section 4, where it briefly obtains a value of roughly 1. Therefore the linear response is expected to be formally valid through most of the plasma and likely adequate for all cases considered.

The general workflow is described by the diagram in figure 2. Equilibrium and coil information from a single time in a discharge is used to calculate the plasma response to a single-n from a Fourier expansion of the applied 3D fields. The 3D perturbed density profile combined with equilibrium profiles is then used to calculate a beam ion birth profile. Inclusion of the perturbed density profile [4, 19–21] is an important effect since it can cause a change in the number of particles deposited at large radii, where particles are most likely to be sourced that hit the wall. Particles from the beam ion birth profile are then followed in the M3D-C1 calculated non-axisymmetric magnetic fields. For simulations of the impact on prompt loss, orbits are followed for one or more bounce periods and particles are considered to hit the FILD detectors if they come within 5 cm (approximately a full energy Larmor radius) of the detector slit. For long timescale simulations used to calculate the new confined EP profile, particles are introduced at a fixed rate and followed for slowing
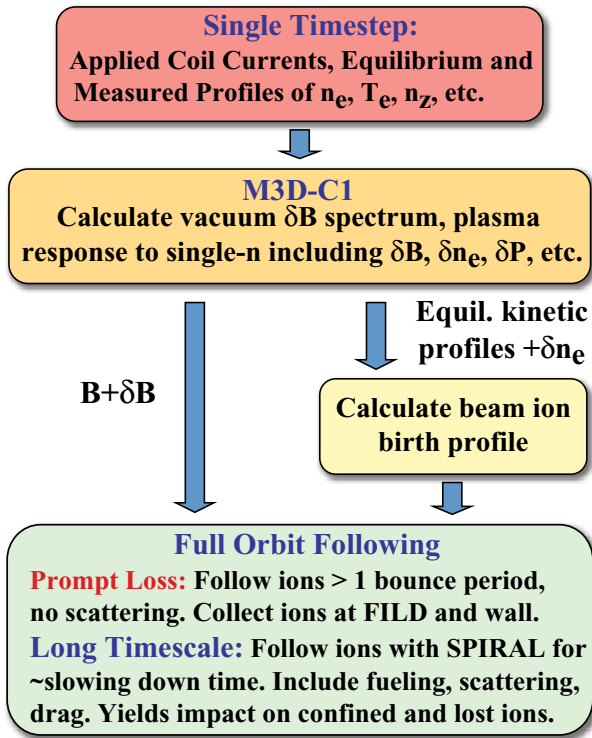
3D Field + Fast Ion Modeling Workflow

Single Timestep:
Applied Coil Currents, Equilibrium and Measured Profiles of n_e, T_e, n_z, etc.

M3D-C1
Calculate vacuum δB spectrum, plasma response to single-n including δB, δn_e, δP, etc.

B+δB

Equil. kinetic profiles +δn_e

Calculate beam ion birth profile

Full Orbit Following
Prompt Loss: Follow ions > 1 bounce period, no scattering. Collect ions at FILD and wall.
Long Timescale: Follow ions with SPIRAL for ~slowing down time. Include fueling, scattering, drag. Yields impact on confined and lost ions.

Figure 2. Workflow for modeling impact of applied 3D fields on fast ion confinement in DIII-D.

Figure 3. Sample beam ion birth profile from $n = 2$ L-mode experiments. (*a*) Birth profile overlaid on M3D-C1 calculated perturbed density profile. White dashed line is axisymmetric LCFS. (*b*) Profiles of electron density, electron temperature, and 80 keV beam neutral profile (red) to mid-radius along with corresponding beam ion birthrate (blue). Both beam neutral and birthrate are arbitrary scales. $\rho = 1$ is the unperturbed LCFS position. (*c*) Top view of the tokamak showing the beam ion birth profile from the 30L beam. Red indicates particles born past the tangency radius. (*d*) Birth pitch distribution of particles.

down timescales using the SPIRAL [22] code which includes the effects of Coulomb drag and pitch-angle scattering. In both types of simulations, particles are considered lost if their trajectory intersects a 3D model for the DIII D inner wall. To simulate rotation of the 3D field, as in figure 1, the process is repeated with the M3D-C1 perturbed profiles rotated by the desired amount.

The beam ion birth profile is calculated using a similar approach to that employed in NUBEAM [23] and FIDASIM [24]; this module, however, is unique in that it allows arbitrary 3D kinetic profiles such as those from M3D-C1 and naturally includes profiles outside the last closed flux surface (LCFS). Each beam is broken into several rays on which profiles of density, temperature, and impurity density are interpolated. The attenuation for a given energy and species along each ray is calculated using ADAS beam stopping cross-sections [25] and from this attenuation profile, the probability for birth along a given ray is derived. A Monte Carlo selection process is used to first pick a ray from a given beam, then a position along the ray. An example full-energy birth profile for the 30L beam is shown in figure 3 where figure 3(*a*) shows the particle birth locations over an M3D-C1 perturbed density profile at a given toroidal location. From figure 3(*a*) it is clear particles can be born outside of the axisymmetric LCFS. The equilibrium profiles of electron density (n_e) and electron temperature (T_e) for the $n = 2$ L-mode discharges presented in the next section are shown in figure 3(*b*), overlaid with an 80 keV beam neutral attenuation profile (red) to mid-radius along with corresponding beam ion birthrate (blue). Retaining
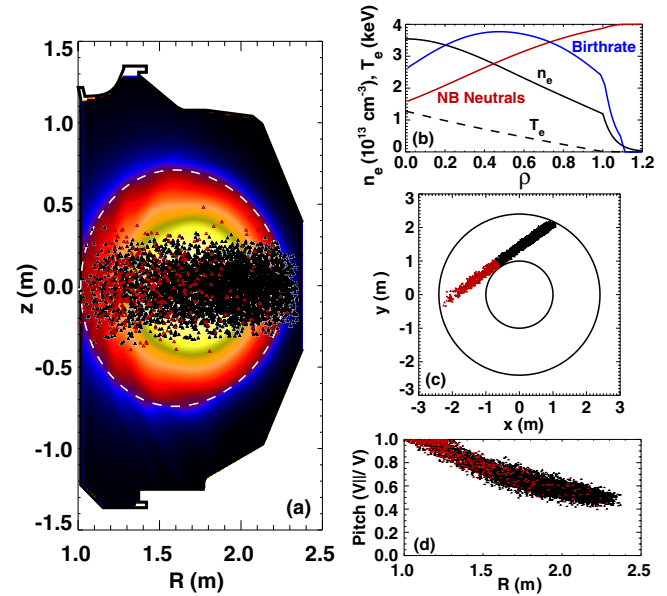
particles born outside the LCFS is essential to proper modeling of this problem (as will be discussed later). In fact, even for axisymmetric investigations, typically 3%–5% of particles are found to be born in this region, yet this important effect is not included in most transport analysis codes.

3. 3D field impact on prompt beam ion loss, $n = 2$ L-mode discharge

In this experiment, a slowly rotating up/down symmetric (even parity) $n = 2$ magnetic perturbation was applied to a low-elongation ($\kappa \approx 1.16$), low-current ($I_p = 0.6$ MA) L-mode plasma with toroidal field $B_T = 2.0$ T and normalized beta $\beta_N < 1$. The discharge was heated by two separate approximately 80 keV neutral deuterium beams, one co-current (30L) and the other counter-current (210L). Low elongation was used to make it easier for orbits to intersect the midplane FILD detector; in more elongated plasmas, EP losses typically intersect the outer wall well below the midplane FILD. The time history of the midplane FILD and a 25 Hz I-coil traveling waveform are shown in figure 1. The FILD signal clearly exhibits modulation of the fast ion losses at the I-coil waveform frequency along with several other features. The overall FILD signal is changing dramatically over the time window shown as a result of the beam timing, current penetration/q-profile evolution and density evolution [4]. During the first phase of the discharge, the plasma was heated predominantly by the counter-current
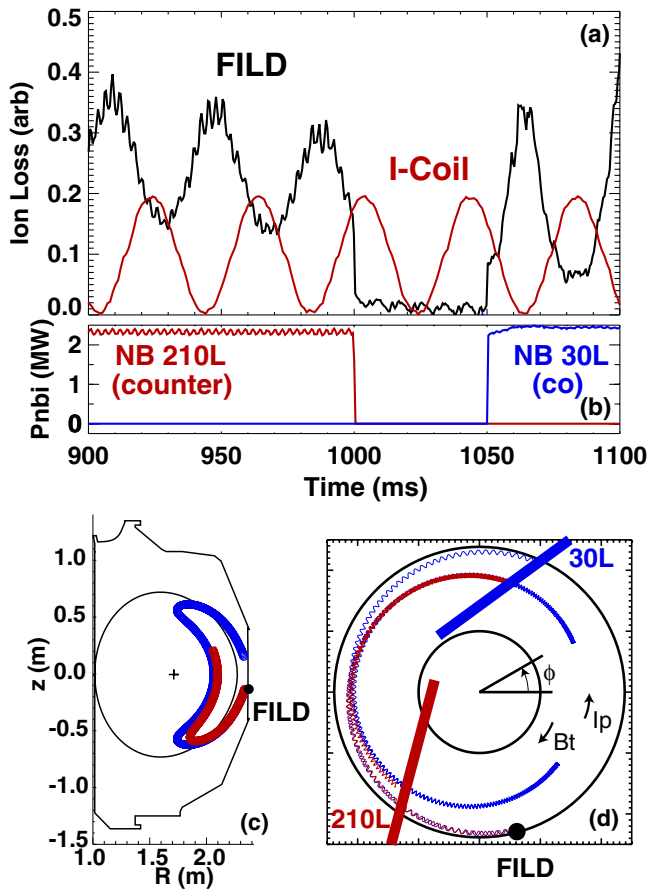
Figure 4. Discharge 146121. Expanded region of figure 1. (*a*) FILD and I-coil time traces. (*b*) 210L and 30L neutral beam waveforms. (*c*) Poloidal projection of reverse orbit following from the FILD to beam overlap for typical prompt loss trajectories from the 210L (red) and 30L (blue) beams. (*d*) Toroidal trajectories for the orbits in (*c*) as well as corresponding beam trajectories.

beam injection (210L) with short blips of the 30L co-current beam for diagnostic purposes. At $t = 1000$ ms, there is a short period during which no beam heating is applied followed by constant injection of only the co-current beam.

The analysis in this paper focuses on the time period near $t = 1000$ ms, an expansion of which is shown in figure 4(*a*). Before $t = 1000$ ms, when the 210L beam is being injected, loss to FILD is observed which terminates rapidly during the 50 ms Ohmic phase. After the Ohmic phase, the co-current 30L beam begins injection and loss is again observed to the midplane FILD, with a larger amplitude modulation. The fact that the losses decay almost immediately following turn-off of the 210L beam indicates that the losses are predominantly prompt in nature, i.e. beam neutrals are ionized and hit the FILD detectors within approximately one poloidal transit. In fact, if one zooms in further on the decay, the FILD signal is observed to decay in < 20 μs after beam turn-off, whereas typical bounce periods for these orbits are ≈ 40 μs. Further evidence that the observed loss is prompt is the fact that small power oscillations in the 210L beam power at 36 Hz show up directly in the measured loss signals. If these signals were due to losses of beam ions that were previously confined or had experienced significant slowing down, these oscillations would be washed out [4].

Reverse orbit tracing of the unperturbed orbits from the FILD location combined with the measured velocity pitch angles can be used to find the approximate birth location and trajectories of the observed ions. The orbit-following results are given in figures 4(*b*) and (*c*), where the orbits were followed backward in time from the FILD until they overlapped with the corresponding beam. From figures 4(*b*) and (*c*), it is clear that counter beam ions promptly lost to FILD must be born inside the LCFS near mid-radius and co-going beam ions are born outside the LCFS. Thus, to properly model FILD measurements of co-going beam ions in these discharges, beam ionization in the scrape-off-layer (SOL) *must* be taken into account.

To simulate this experiment, the prompt loss to FILD was calculated for ten different phases of the $n = 2$ perturbation with 250 000 particles followed at each phase. As mentioned in the previous section, particles that come within 5 cm of FILD were considered to have hit the detector. Modeling results show the typical orbits are very similar to their unperturbed trapped orbits but are modulated radially by approximately $+/-1$ cm on their first poloidal transit [4] causing orbits from different birth positions to connect to the FILD detector at a given time (phase of the $n = 2$ perturbation). Since gradients exist in the ionization profile at the birth positions, this causes an oscillation in the measured loss signal [26]. To compare the experimental data directly to simulation, the midplane FILD data are mapped from time to the equivalent phase of the $n = 2$ perturbation (*n*2 phase) used in the simulations and scaled by the average FILD signal over one cycle—the results of which are shown in figure 5 [4]. The modeling results in figure 5(*b*) include both the perturbed birth profile and $n = 2$ magnetic field with plasma response. Modeling captures many of the features apparent in the FILD data: larger modulation of 30L losses as compared to 210L, 30L losses peak near *n*2phase $= 0$, and an approximate 30 Deg phase shift between 30L and 210L loss modulation is also observed as in experiment. The depth of modulation from simulation, however, is smaller than that observed experimentally. There are several potential reasons for this disagreement, the first is that the modeling includes only the $n = 2$ contribution to the perturbed magnetic fields. Due to the finite number of coils in each row (six) there is a significant $n = 4$ contribution that, in vacuum, can be up to half the amplitude of the $n = 2$ fields. An indication that this may be significant is apparent in the 30L FILD data in figure 5, where the modulation is clearly asymmetric about the mean and not sinusoidal as the modeling predicts. Another factor that can contribute to the difference is that the FILD data include losses from full, half, and third energy components whereas modeling has only been carried out for the full energy component of the losses. Simulations were also run for 4X the duration of those shown in figure 5 to check whether including more bounce periods could change the depth of modulation with the result that no significant difference was found. Interestingly, while the results in figure 5 show a local increase/decrease in prompt loss at the FILD detector about the mean, the simulations actually point to an overall increase in *total* prompt loss due to the presence of the $n = 2$ fields, with the level of increase dependent on the phase of the perturbation relative to the beam injection location.
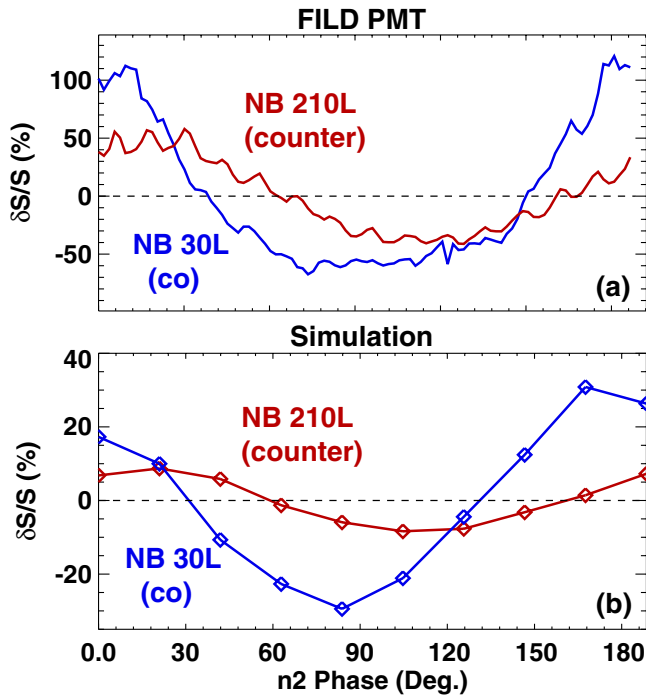
Figure 5. DIII-D discharge 146121. (*a*) FILD PMT data from 30L (blue) and 210L (red) mapped to the equivalent phase of the $n = 2$ perturbation. Data from 40 ms interval centered at $t = 965$ ms and $t = 1070$ ms for the 210L and 30L beams, respectively. Data are expressed as the difference from the mean (δS), divided by the mean (S) over the 40 ms interval. (*b*) Full orbit following simulation results for expected modulation.

4. 3D field induced fast ion transport in $n = 3$ RMP ELM suppressed plasmas

One of the primary motivations for the inclusion of 3D field coils in future tokamaks is the mitigation of ELMs [27]. In 2013, preliminary simulations of the expected fast ion transport in a typical DIII-D $n = 3$ RMP ELM suppressed plasma were carried out. These simulations predicted a significant reduction in the edge fast ion profile due to the presence of the $n = 3$ fields. In 2014, an experiment was carried out to investigate this effect. In the experiment, an ITER Similar Shape (ISS) [28] plasma was created with an odd-parity $n = 3$ field, $q_{95} = 3.47$, pedestal density $n_{e-ped} \approx 1.4 \times 10^{19}$ cm^{-3}, and short 50 ms I-coil off periods to allow the fast ion profile to recover without loss of ELM suppression. Maintaining ELM suppression was a key part of this experiment since the ELMs themselves can cause significant edge fast ion transport as well as compromise FIDA measurements of the edge EP density by inducing large changes in the background. Time histories of the D-alpha emission, line-averaged density, and I-coil current are given in figure 6, along with the FIDA beam waveform. After density pumpout, ELM suppression is obtained near $t = 2800$ ms and maintained throughout each of the short I-coil off periods. During each off-period, the density begins to rise as expected but the pedestal remains below the threshold for ELMs to return.

FIDA measurements throughout the I-coil off periods show an increase in edge FIDA density then a return to lower levels
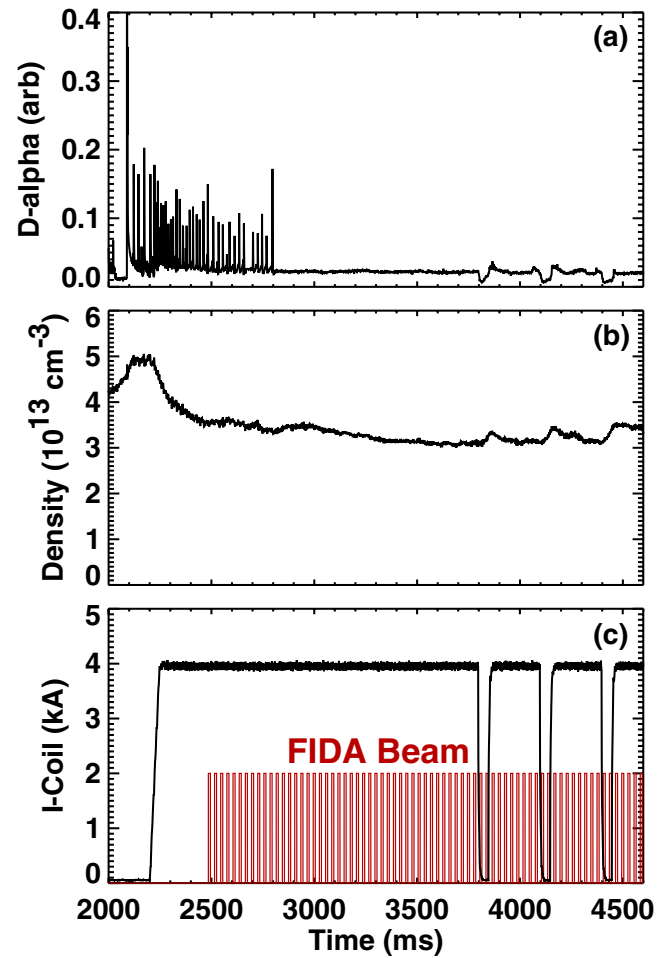

Figure 6. DIII-D discharge 157545. Timetraces of (*a*) fast D_α photodiode. (*b*) Line-averaged density. (*c*) I-coil current (black), active beam for FIDA diagnosis (red).

after the $n = 3$ fields are switched back on. An example of the FIDA evolution throughout an $n = 3$ off-pulse is shown in figure 7, where it is seen that the edge FIDA emission can increase by up to a factor of two or more during the $n = 3$ off period, indicating a large change in the edge fast ion density. The particular edge FIDA channels shown correspond to primarily co-passing ions with energies > 25 keV.

In the same discharges, a wide field-of-view infrared periscope was used to measure the heating of the vessel first wall. Infrared periscope images show localized heating due to several fast ion related sources as well as a significant change in heat flux correlated with the I-coil off-pulses. Heat flux images calculated from infrared camera measurements of the wall temperatures are shown before (figure 8(*a*)) and during (figure 8(*b*)) an $n = 3$ off-pulse. Three separate regions are highlighted in figure 8(*a*). These correspond to: (1) localized heating predominantly synchronized with the 210R counter current beam, a result of prompt beam ion loss [29], (2) heating of the center post due to 150R beam shine-through, (3) a large divertor heat flux that is reduced during the RMP off-phases. Changes in divertor heat load due to loss of the thermal plasma during application of non-axisymmetric fields has been studied in this regime previously, where it was
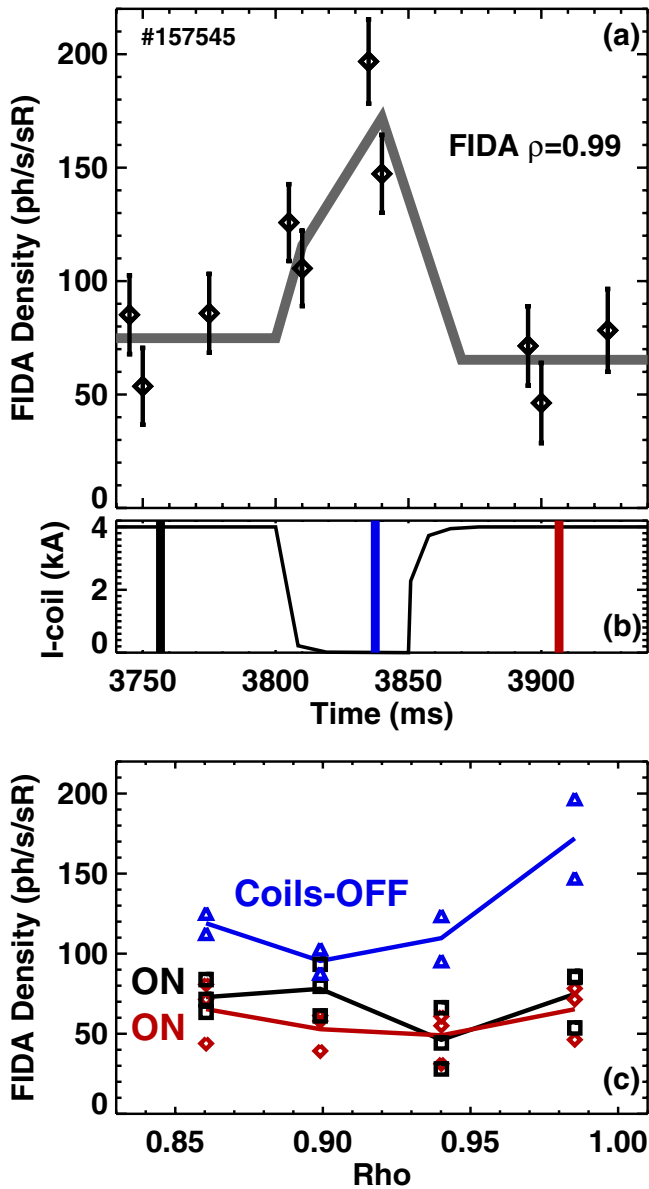
Figure 7. DIII-D discharge 157545, edge FIDA data. (*a*) Time histories of FIDA density throughout $n = 3$ off-period at $\rho \approx 0.99$. (*b*) I-coil waveform. (*c*) FIDA density profiles before, during, after $n = 3$ off-period corresponding to times of vertical black, blue, and red bars respectively in panel (*b*).

Figure 8. Heat flux in 157418 calculated from infrared periscope measurements. (*a*) $n = 3$ ON. Dashed green lines indicate: region 1 = primarily prompt loss from 210R counter beam. 2 = Shine-through heating from 150R beam, 3 = Divertor heat load. (*b*) $n = 3$ off. Black rectangle indicates blocked view.

shown that particle drifts can play a large role in the resulting loss patterns [30]. Much of the divertor heat load was shown to be from thermal ion loss with higher energy ions reaching further from the calculated field line strike points. The same is certainly true for fast ion loss; it is expected that both will contribute to the divertor heat load and, in fact, the drift effects will be larger for fast ions.

Full slowing-down timescale SPIRAL simulations of the $n = 3$ induced fast ion transport have been carried out for discharge 157418. In the simulations, beam ions were injected at a constant rate over a 180 ms period. After a full slowing down steady-state distribution was built up (~70 ms), $n = 3$ fields were turned on, then after another 30 ms, an experimental $n = 3$ off-pulse was included in the simulations during which, the $n = 3$ amplitude was scaled by the I-coil current waveform
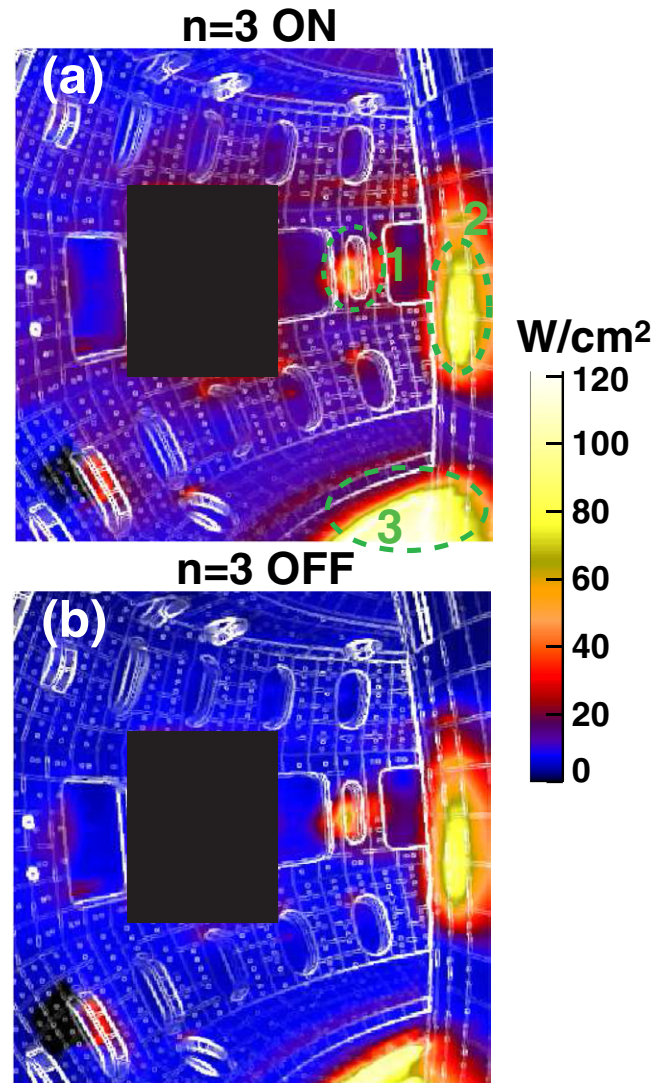
shown in figure 9(*b*). In figure 9(*a*), the lost power normalized to injected beam power is shown versus time (loss is defined as hitting the vessel wall before thermalization). When the $n = 3$ fields are turned on at $t = 0$, a large jump in EP loss occurs as previously confined particles, which are now on unconfined orbits, are rapidly lost. After approximately 7 ms, a new steady-state loss rate is reached that is roughly three times that of the case without $n = 3$ fields. During the 50 ms off-pulse, the losses rapidly reach the no-coil level and following the slower I-coil turn-on at $t = 80$ ms, the spike up in predicted power loss reaches lower peak values but reaches the same steady-state loss rate. In steady-state, with $n = 3$ fields applied, 8.4% of the injected beam power is lost in the simulations compared to 2.7% without $n = 3$ fields. Figure 9(*c*) shows the confined steady-state fast ion profile ($t = 23$ ms) in the simulations. From this figure, it is clear that the lost particles are coming from minor radii outside of $\rho \approx 0.7$ (ρ = normalized square-root of toroidal flux), where the $n = 3$
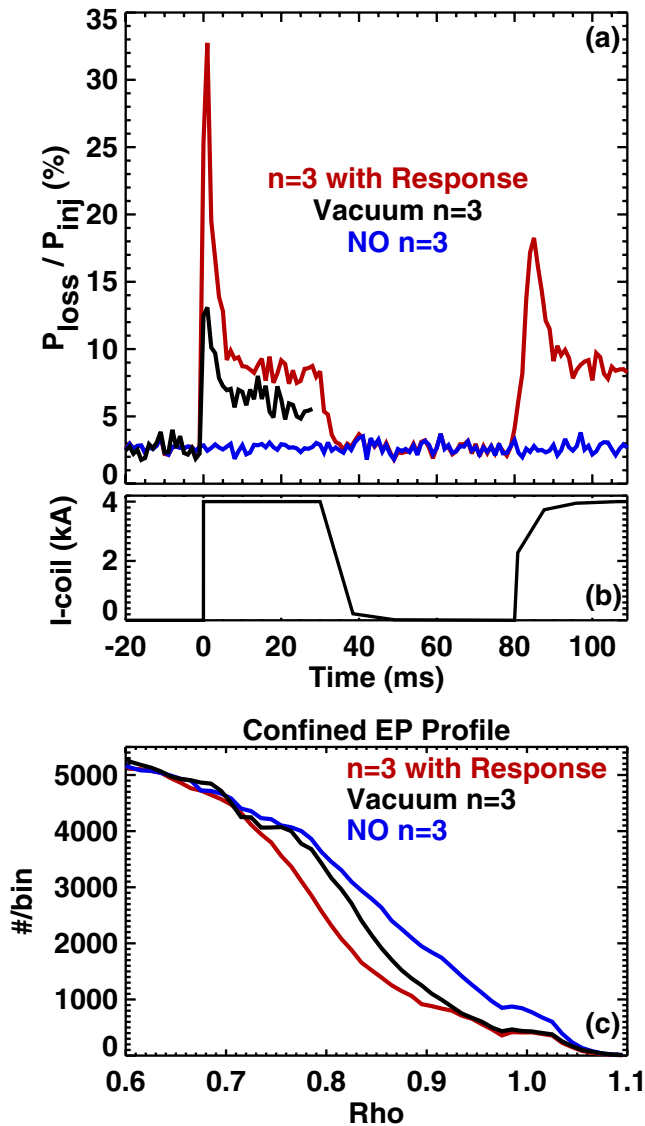
Figure 9. SPIRAL simulations of DIII-D discharge 157418. (*a*) Lost beam power normalized to injected power in ~1 ms bins for simulations with $n = 3$ fields including plasma response (red), vacuum $n = 3$ fields only (black), and axisymmetric fields only (blue). (*b*) I-coil current used in simulations with $n = 3$ fields in panel (*a*). (*c*) Steady-state confined EP radial profile at $t = 23$ ms in simulations.
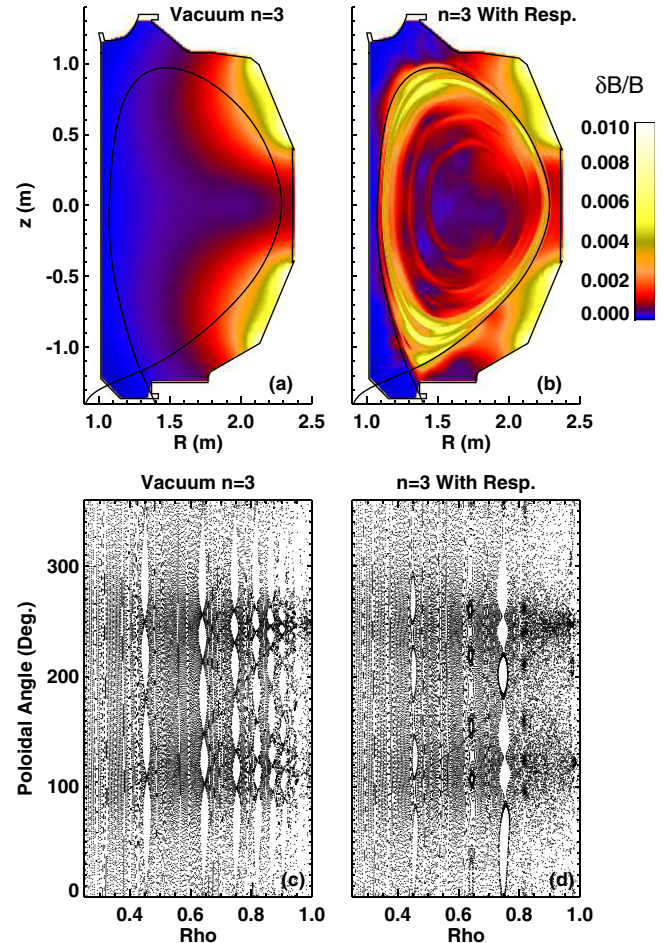
Figure 10. (*a*) Peak amplitude of $n = 3$ component of applied vacuum magnetic field in discharge 157418. Amplitudes are scaled to the local magnetic field. (*b*) Amplitude of M3D-C1 calculated response + applied $n = 3$ field. (*c*) and (*d*) Poincare plots at $\varphi = 60$ deg. for vacuum $n = 3$ and with applied + plasma response respectively.

fields are observed to induce up to a 55% deficit in the local confined fast ion profile ($\rho \approx 0.95$) and a 5.1% reduction in the total number of confined fast ions. This is consistent with the large drop in FIDA density observed in figure 7, a more detailed comparison of which will be made in following sections using the FIDASIM code [24] combined with SPIRAL calculations.

Also included in figure 9 are SPIRAL simulations carried out using the applied vacuum $n = 3$ spectrum with no plasma response. The resulting power loss is significantly lower than that with the full plasma response included but elevated compared to the no $n = 3$ case. The steady-state loss rates are $\mathrm{Ploss_{with\ resp.}}/\mathrm{Ploss_{vacuum}}/\mathrm{Ploss_{NO \sim n=3}} = 8.4$ %/6.0%/2.7%. From figure 9(*c*), it is seen that the resulting EP profile for the vacuum $n = 3$ case is very similar to that

with response included outside of $\rho = 0.92$ but returns to the classical no-coil case faster and the profile inside of $\rho \approx 0.8$ is only weakly affected. This difference can be explained when one compares the predicted non-axisymmetric fields with and without plasma response included. This comparison is given in figure 10, where the vacuum $n = 3$ field amplitude scaled to the local equilibrium field is shown in figure 10(*a*) and that with plasma response included in figure 10(*b*). The fields with plasma response included have more structure (as expected) as well as regions of significantly higher amplitude inside the core plasma. Poincare plots at $\varphi = 60$ deg. are shown for the vacuum and response case in figures 10(*c*) and (*d*) respectively, where the poloidal angle in the figure begins at the outboard midplane and increases in the counter-clockwise direction. Both cases have regions of stochastic fields, however, for the case with plasma response included, the stochastic regions appear to extend to $\rho \approx 0.8$, whereas only $\rho \approx 0.95$ for the vacuum $n = 3$ case. Clearly, the plasma response significantly alters the fields the particles feel, can alter the transport, and must be included in modeling. All subsequent analysis presented here focuses on runs with plasma response included.
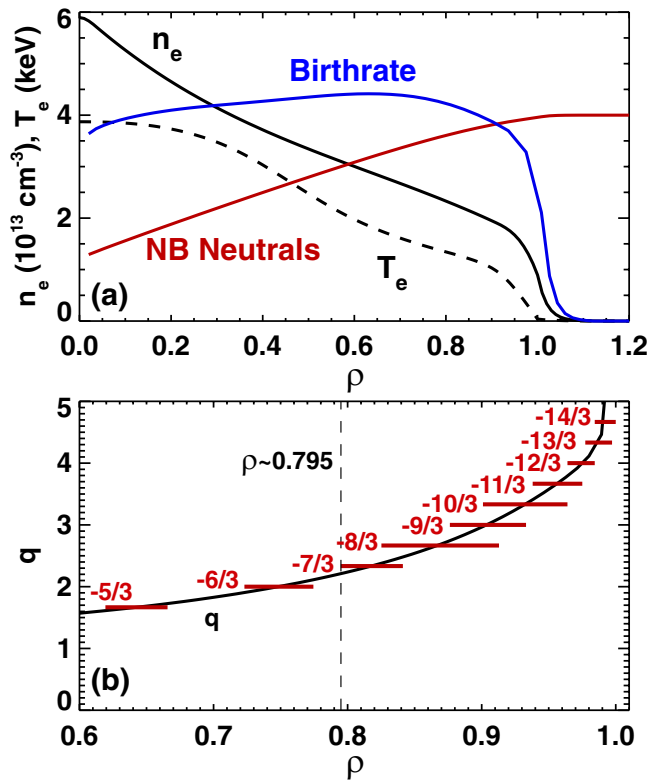
Figure 11. Discharge 157418 with $n = 3$ RMP on. (*a*) Profiles of electron density, electron temperature, and 80 keV beam neutral profile (red) to mid-radius along with corresponding beam ion birthrate (blue). Both beam neutral and birthrate are arbitrary scales. $\rho = 1$ is the unperturbed LCFS position. (*b*) Outer q-profile overlaid with calculations of island size for the M3D-C1 case with plasma response included (figures 10(*b*) and (*d*)). Vertical line at $\rho = 0.795$ indicates break in the island chain.

Figure 12. SPIRAL simulations. (*a*) Confined distribution function for particles at $\rho > 0.7$ and no applied 3D field. (*b*) Confined distribution function for particles at $\rho > 0.7$ with the $n = 3$ field applied. (*c*) Difference between panels (*b*) and (*a*).

As with the $n = 2$ L-mode discharge, relevant kinetic profiles extending into the SOL from the $n = 3$ RMP ELM suppression plasma are given in figure 11, where profiles of electron density, electron temperature, and 80 keV beam neutral profile (red) to mid-radius along with corresponding beam ion birthrate (blue) are shown. Figure 11(*b*) shows the safety factor profile (q) for the same time overlaid with SURFMN [31] calculations of island size for the M3D-C1 case with plasma response included (figure 10(*b*) and (*d*)). The vertical line at $\rho = 0.795$ indicates break in island chain and the approximate inner extend of the stochastic region discussed in the previous paragraph.

The SPIRAL calculated fast ion distribution function for all confined particles with $\rho > 0.7$, is shown in figure 12(*a*) (classical no $n = 3$ case) and figure 12(*b*) ($n = 3$ with plasma response). The difference due to the $n = 3$ fields is given in figure 12(*c*). Roughly, all particles in figure 12 with $|V_{\parallel}/V| > 0.6$ are passing particles. Clearly, the biggest change in the distribution function occurs for co-passing (pitch>0) fast ions and the drop extends to the highest energies. Fortunately, this is the same region of phase space probed by the edge FIDA channels shown in figure 7. At lower energies ($E < 25$ keV), some change in the lower pitch angles corresponding to trapped orbits occurs as well. This preferential drop in far
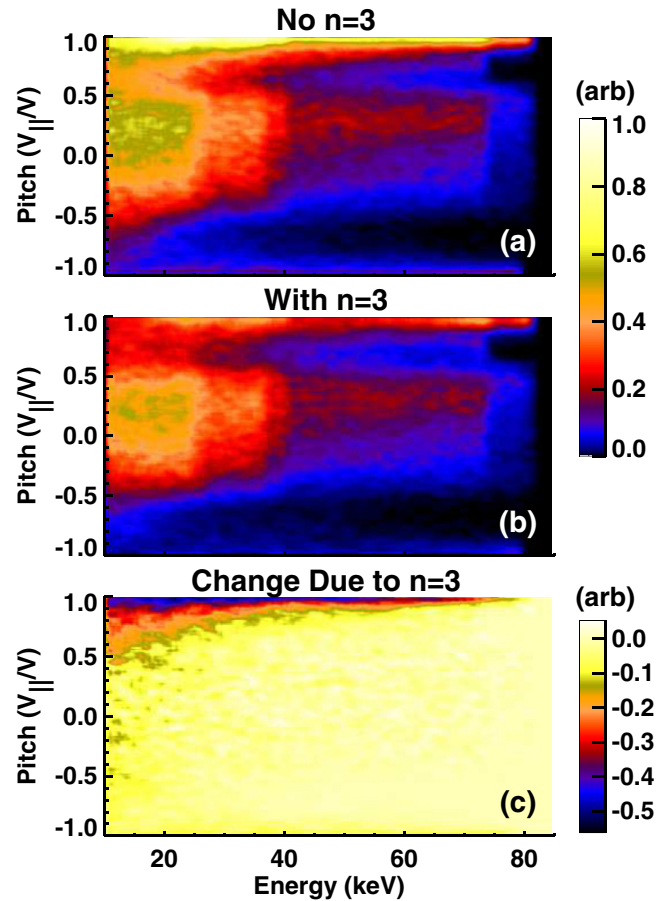
passing particles can be expected for stochastic fields such as those in figure 10(*d*).

Further details of the lost particles can be seen in figure 13, where the lost particles' birth ($\times$) and final ($\diamond$) poloidal positions are shown. As can be seen from this figure, the majority of lost particles strike the wall in the divertor region, consistent with the location of the largest changes observed on the IR periscope. The losses shown in figure 13 are broken into four classes, those injected by the co- and counter-current beams and further divided by their birth location, on the high-field side (HFS) or low-field side (LFS) of the magnetic axis. Almost all beam ions born on the HFS of the magnetic axis are born onto passing orbits—seeding the part of the distribution function in figure 12 found to be most affected by the $n = 3$ fields. Co-injected beam ions then travel counter-clockwise poloidally and end up near the inner leg of the separatrix. An example of this type of loss orbit is overlaid as a green solid curve in figure 13(*a*), where the guiding center of the full orbit calculation is shown. These lost passing orbits represent the primary loss of higher energy beam ions and are due to the stochastic fields shown in figure 10(*d*) and discussed further in the context of island overlap in figure 11(*b*). The orbits do not undergo an orbit transformation in the loss process, rather, they remain passing as they traverse the stochastic magnetic field
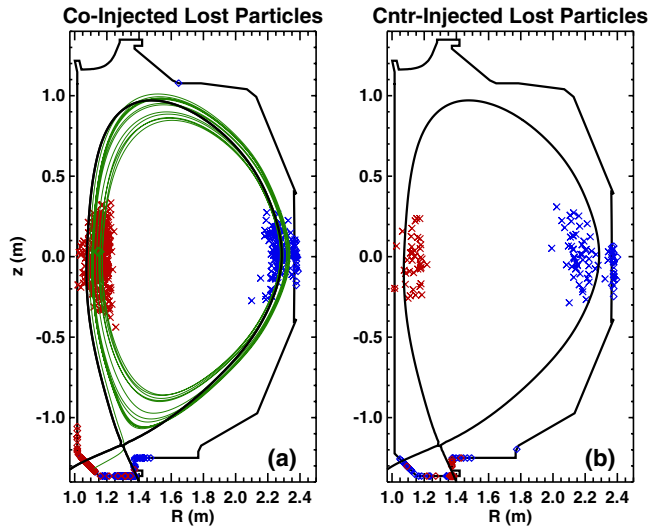
Figure 13. Initial and final positions of lost particles injected at full energy due to $n = 3$ RMP. (*a*) Co-current injected beam ions. Green overlay is the guiding center of typical co-injected passing ion that is lost to the inner divertor. (*b*) Counter-current injected beam ions. X = initial position, diamond = final. Blue/red = HFS/LFS birth locations, respectively.

region until they are lost to the divertor. Similarly, counter-injected passing ions born on the HFS travel clockwise and end up primarily near the outer portion of the divertor. Not shown, but indicated by the few transits made in the example orbit, is the fact that these passing losses are primarily near the injection energy. Losses from the LFS of the magnetic axis are particles that are born onto primarily trapped orbits and remain on trapped orbits until they are eventually lost. These can span the divertor region when lost, but for co-injected particles, the losses are primarily concentrated in the outer portion of the divertor and only occur after the particles have slowed down to lower energies $E \approx 25$ keV and deposited a significant fraction of their energy. The loss of particles born on the HFS of the magnetic axis leads one to believe much of the divertor heat load due to EP loss could be ameliorated by raising the central electron density. With low densities (3.5×10^{13} cm^{-3}) such as in these RMP ELM suppressed plasmas, the beam penetration is larger and a significant fraction of particles are born at large minor radii on the HFS. Indeed, preliminary investigation of the heat load between ELMs before density pumpout is complete shows a reduction in divertor heat loads on the inner leg.

As mentioned, the majority (up to 70%) of the lost particles in the SPIRAL simulations strike the divertor region. Figure 14(*a*) shows a zoomed in diagram of the divertor surface with overlaid boxes proportional in size to the number of particles per unit length striking that particular region. Overlaid on the figure are the axisymmetric inner and outer strike points. Graphically, from this figure, it is clear that the majority of particles strike inside the private flux region just below the inner strike point. The toroidally averaged heatflux along the divertor surface is shown in figure 14(*b*) versus major radius, where the peak heat flux immediately after the abrupt $n = 3$ turn-on ($t \approx 1$ ms in figure 9(*a*), after the experimental off-pulse ($t \approx 85$ ms in figure 9(*a*), and steady-state with and without $n = 3$ are given.
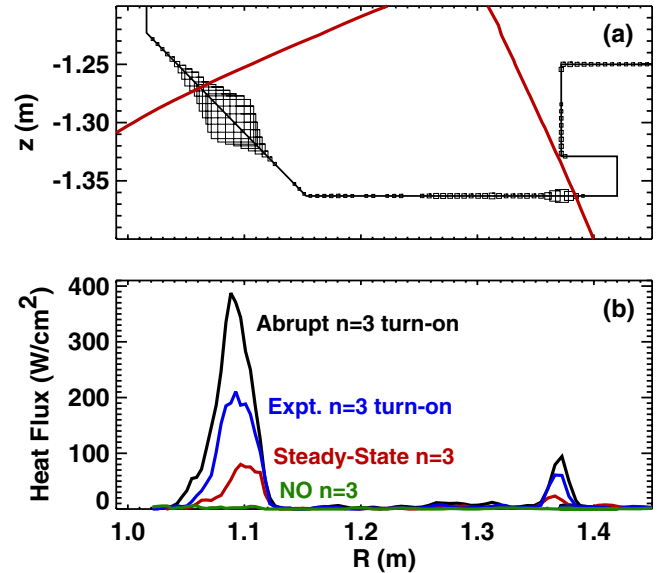

Figure 14. SPIRAL calculations. (*a*) Loss position in divertor region during abrupt $n = 3$ turn-on at $t = 0$ ms in figure 9. Box size scaled to represent the number of particles striking the corresponding region of wall. (*b*) Toroidally averaged EP heat flux in the divertor region: peak immediately after abrupt turn-on (black), peak immediately after slow turn-on using experimental I-coil current waveform (blue), steady-state heat flux with $n = 3$ applied (red), heat flux with no $n = 3$ applied (green). Averaging time is 1 ms and spatial averaging distance along the wall is 1.5 cm.

In the unphysical instantaneous turn-on case, the peak toroidally averaged heat flux can reach up to 390 W cm^{-2} whereas with the experimental $n = 3$ turn-on, the peak heat flux is approximately half that at 200 W cm^{-2}. The peak steady-state heat flux is 40% that immediately following turn-on and reaches 80 W cm^{-2}. For comparison, with no $n = 3$, the divertor EP induced heat flux is <10 W cm^{-2}. Toroidally, some $n = 3$ structure to the simulated divertor heat flux exists so actual peak values will be larger than the toroidal average quoted above. Additionally, what is not shown is that the higher energy particles hit the divertor surface further from the unperturbed strike point location than lower energy particles, something consistent with calculations presented for thermal particles in reference [30]. It is interesting to point out the SPIRAL simulations presented here, showing loss predominantly to the divertor region, are similar to simulations presented in reference [32] for 3D field induced EP loss in ITER. In those simulations, however, it was found the losses are primarily of trapped particles whereas for the case presented here, the dominant loss is of passing particles.

The 'FIDA density' reported in figure 7 is an approximation to local fast ion density in a specific region of phase space determined by the diagnostic weighting and gives a useful measure of the evolution of the edge EP profile throughout the $n = 3$ off-pulses. It is possible, however, for other factors such as changing profiles of electron density, electron and ion temperature, Z_{eff}, etc to also complicate the measurement. As expected, and as can be seen from the evolution of the line-averaged electron density in figure 6(*b*), the kinetic profiles are evolving somewhat during each of the $n = 3$ off-pulses. To evaluate whether or not the evolving kinetic profiles throughout the off-pulses is contributing to the change in FIDA emission and
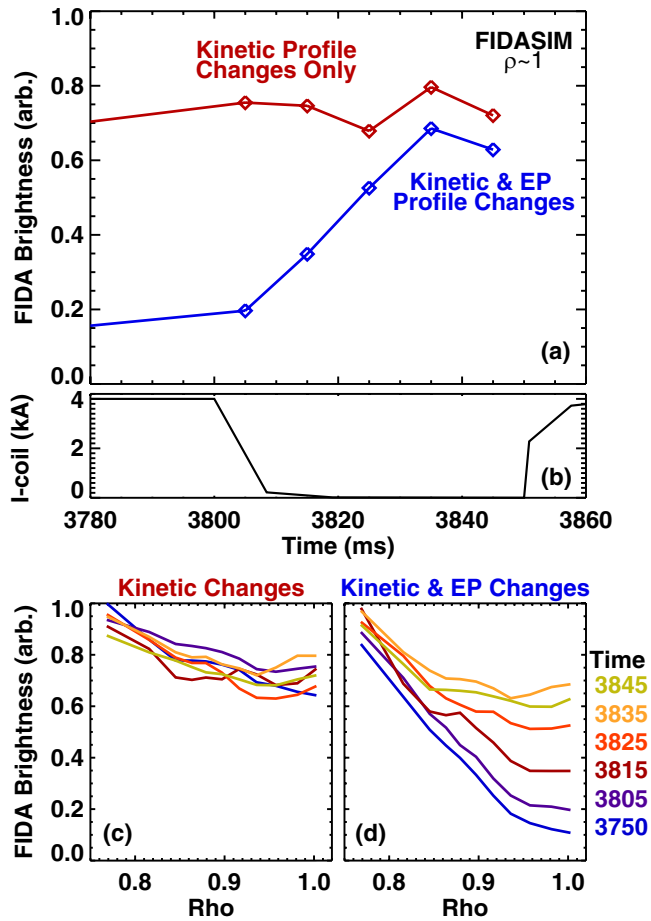
Figure 15. FIDASIM calculations for discharge 157545. (*a*) FIDA brightness evolution for a FIDA chord viewing $\rho \approx 1$ integrated over the same wavelength range as the FIDA data presented in figure 7. Red points are for simulations using only the measured evolving kinetic profiles and blue include both evolving kinetic profiles as well as SPIRAL calculated EP profile evolution due to the applied $n = 3$ field with a current waveform from panel (*b*). (*c*) and (*d*) Radial FIDA brightness profile evolution for tangential viewing FIDA chords (*c*) with and (*d*) without an EP profile evolved in the presence of $n = 3$ fields.
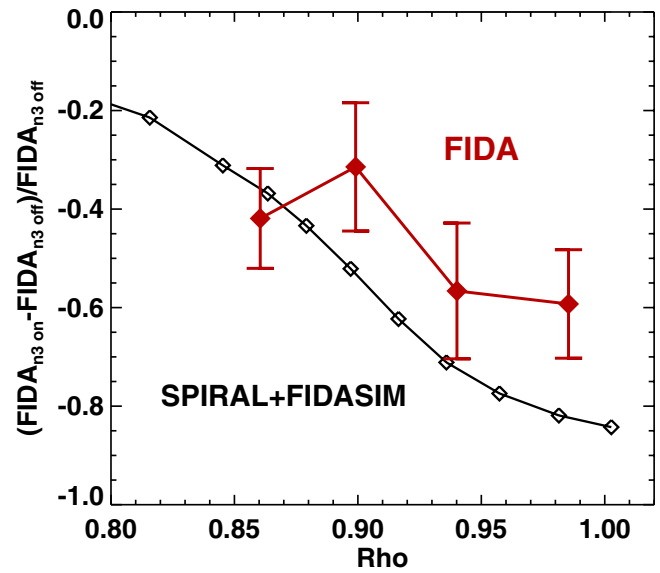

Figure 16. (black) FIDASIM calculations of the expected change in FIDA signals during an $n = 3$ off-pulse using SPIRAL calculated EP distribution functions. (red) Measured change in FIDA signals during an $n = 3$ off-pulse in 157545.

is obvious the evolving kinetic profiles cannot cause the large measured change in edge FIDA signals and that the measured change is likely due to an evolving EP profile. Figure 16 shows a comparison of the measured change in FIDA signal during an $n = 3$ off-pulse to that from combined FIDASIM and SPIRAL calculations for the four edge FIDA chords. Reasonable agreement is shown, however, the predicted depletion of the edge FIDA emission is slightly larger at the LCFS than measured. As a reminder, for these experiments and proof of principle, only four of the edge charge exchange recombination (CER) chords typically used for carbon measurements were tuned to the FIDA wavelength range. Future experiments will tune the entire array to FIDA to more than double the number of points as well as extend these measurements further into the core where the signal is expected to return to classical levels.

5. Future work—resonances between applied 3D fields and fast ion orbits as an EP actuator

Interestingly, not all effects of symmetry-breaking fields on EPs are detrimental [33–35]. One recent experimental example shows applied $n = 3$ perturbations could potentially be used as a means to alter EP-driven instabilities by interacting with the regions of phase space that are responsible for driving the modes [33]. A key element of future energetic particle work on DIII-D is not only being able to predict the impact of instabilities and 3D fields on energetic particles but developing actuators to exert targeted control over the EP profile (in both configurational and velocity space) and ideally reducing undesirable phenomena such as large, transport causing instabilities. From this standpoint, the effects observed in the previous sections are interesting because they offer a rare opportunity to make a macroscopic impact on the EP profile in a controlled way with an easily adjusted external
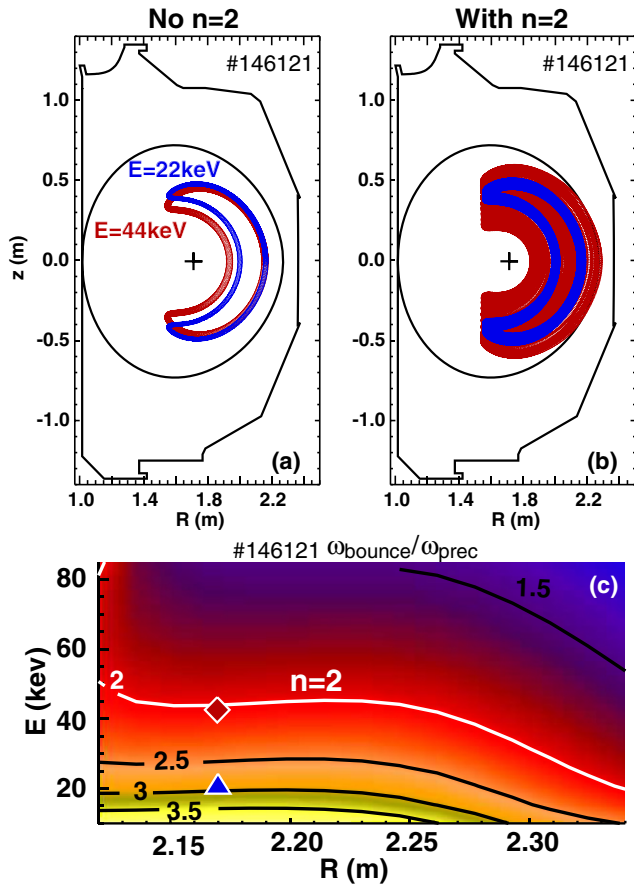
also to compare the predicted change in FIDA emission due to EP transport, FIDASIM calculations were carried out using SPIRAL calculated fast ion distribution functions throughout a representative $n = 3$ off-pulse. FIDASIM [24] is a FIDA modeling code which, given an input distribution function, is capable of calculating the full spectrum and theoretical number of photons observed by each FIDA view chord. The FIDASIM results are shown in figure 15 for SPIRAL calculated fast ion distribution functions with and without $n = 3$ fields. The time evolution of a simulated tangential FIDA channel near $\rho \approx 1$ is shown in figure 15(*a*) for a run with only the measured evolving kinetic profiles and SPIRAL calculations with NO $n = 3$ fields (labelled '*Kinetic Profile Changes Only*') as well as a case with both the evolving kinetic profiles and EP distribution that was calculated using the evolving $n = 3$ fields (labelled '*Kinetic and EP Profile Changes*'). The temporal evolution of the simulated radial FIDA profiles for the two cases are shown in figure 15(*c*) and (*d*). From these simulations, it

Figure 17. (*a*) Unperturbed orbits in 146121. (*b*) Orbits with $n = 2$ field applied at 5 × expt. amplitude. 44 keV particle (red) fulfills the resonance condition. (*c*) Ratio of $\omega_{\text{bounce}}/\omega_{\text{prec}}$ versus energy and radius for center of 30L beam. Initial conditions of 44 and 22 keV orbits in (*a*) and (*b*) overlaid as a diamond and triangle.

Figure 18. Calculated change in toroidal canonical angular momentum (δP_ϕ) due to $n = 2$ fields for particles initialized with given energy, radius and pitch determined by 30L beam geometry. Equilibrium from discharge 146121. Green overlaid curve represents $n = 2$, $l = 1$ resonance using axisymmetric bounce and precession frequencies. Black squares represent lost particles. (*a*)–(*c*) 1,∼2.5,∼ 5 ×experimental amplitude. (*d*)–(*f*) phase of $n = 2$ field shifted by $\delta\phi = \pi/4$, $\pi/2$, $3\pi/4$ respectively.

actuator, i.e. coil current, toroidal mode number, phasing, etc. Having established our ability to realistically model the interaction of fast ions with 3D fields in DIII-D, the question arises, is there some type of more targeted control possible with the currently available hardware and operating space. Preliminary simulations presented in this section show that it is in principle possible for typical operating parameters and the current DIII-D coil set to specifically target parts of EP phase space by taking advantage of resonances with applied 3D fields—it is left for future experiments to search for practical limitations associated with actually measuring and ultimately exploiting these resonances.

It is well known that under certain conditions resonances between fast ion drift orbits and both static and dynamic non-axisymmetric fields can exist [36]. The standard condition for resonance is $\omega = n\omega_{\text{prec}} + l\omega_{\text{bounce}}$, where ω is the frequency of the perturbation, n is the toroidal mode number, ω_{prec} is the fast ion toroidal precession frequency, ω_{bounce} is the poloidal bounce frequency, and l is an integer. For zero frequency modes, the resonance condition is simply $l\omega_{\text{bounce}}/\omega_{\text{prec}} = n$. For low-$n$ perturbations such as those applied here, it is difficult for trapped thermal ions to fulfill this condition without an additional radial electric field induced drift, while fast ions can. Shown in figure 17 is an
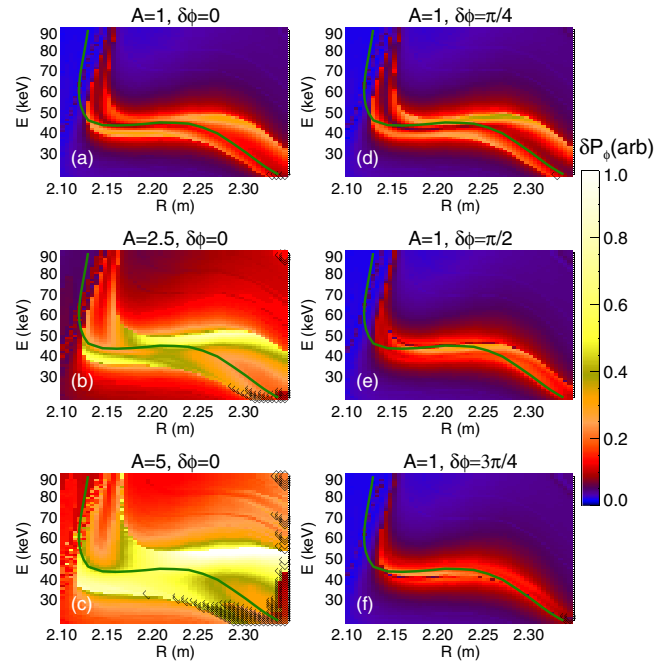
example of the impact of resonance on the motion of a 45 keV ion that fulfills the $n = 2$ resonance condition for the discharge 146121 discussed in section 3. For reference, a 22 keV ion that does not fulfill the condition is also shown. For the particle at resonance, a much larger radial displacement is observed and, with collisions or a loss boundary included, this region of phase space would experience larger transport. Figure 17(*c*) shows contours of the ratio of $\omega_{\text{bounce}}/\omega_{\text{prec}}$ calculated for the particles launched along the outboard midplane with the pitch set by the direction of the 30L neutral beam with respect to the local magnetic field at that radius (the center of the pitch angle distribution generated by the beam). Note the radial electric field has been neglected here as it is a relatively small effect for this low-rotation discharge. The variation of this resonance with radius is a function of the local equilibrium and injection geometry so, by tailoring the current profile, toroidal field, beam, etc the resonances could be placed wherever desired to target specific regions of phase space across the plasma or intentionally tailored to remove resonances and reduce EP transport.

Figure 18 shows calculations of the peak change in toroidal canonical angular (δP_ϕ) after several poloidal transits for particles launched with a range of energies and initial major radius along the outboard mid plane. As in figure 17(*c*), the initial pitch is chosen to match that of the 30L beam at the initial radius. Figures 17(*a*)–(*c*) are for three different $n = 2$ amplitudes—1 × ∼ 2.5 ×, and 5 × the experimental amplitude in 146121 respectively. As the amplitude is increased,

the perturbed δP_φ grows as well as the region over which particles are affected. Additionally, as the amplitude increases, more and more particles are lost (represented by black overlaid diamonds). At the highest amplitude, additional resonant like features appear in the losses which may be related to the fractional resonances presented in reference [37]. Figures 17(*a*), (*d*)–(*f*) represent a scan of the phase of the $n = 2$ perturbation relative to the injected beam ions. From this scan, it is clear the region of phase space affected can be made to move considerably relative to the axisymmetric calculation of the $l\omega_{\text{bounce}}/\omega_{\text{prec}} = n$ resonance location. In fact, in this collisionless limit, one can adjust $\delta\phi$ to have very little to no change along the axisymmetric resonance location. One can imagine adjusting this resonance location and phase such that very small changes would make a resonance possible in the plasma or not for a given beam, particularly if the resonance could be placed very near or just above the injection energy.

6. Conclusions

Measurements and modeling of fast ion transport in DIII-D due to applied 3D magnetic field perturbations have been presented. In an L-mode discharge with a slowly rotating $n = 2$ magnetic perturbation, the dominant observed signature is a modulation of prompt beam ion loss. Full orbit following combined with M3D-C1 calculations of the perturbed fields and kinetic profiles reproduces many features of the measured losses, particularly the phase and relative amplitude of the modulated loss from two different beams. These experiments and simulations show the importance of the phase of the non-axisymmetric perturbation with respect to the injected beams in determining the overall prompt loss level as well as including particle birth in the SOL in modeling of the problem. Extension of the simulations to full slowing-down timescales, including fueling and the effects of drag and pitch angle scattering, show the applied $n = 3$ RMPs in ELM suppressed H-mode plasmas can induce a significant loss of energetic particles from the core. With the applied fields, an additional 5.7% of the injected beam power is lost to the wall beyond that with axisymmetric fields. These particles, originating from minor radii $\rho > 0.7$, are predicted to be primarily co-passing particles lost to the divertor and to a lesser extent the outboard midplane region, consistent with wide field-of-view infrared periscope measurements of wall heating. Edge FIDA measurements in RMP ELM suppressed plasmas also confirm a large reduction in the edge fast ion density due to the applied $n = 3$ fields. FIDASIM calculations using SPIRAL simulations of the modified EP distribution function due to the $n = 3$ fields are consistent with the measured reduction in edge FIDA emission. To reduce divertor heat loads in these RMP ELM suppressed plasmas, two obvious suggestions are: operate at the highest density possible at which ELM suppression can be maintained (to increase beam attenuation and reduce deposition of passing particles born on the HFS at large

minor radius), and ramp coil currents up as slowly as possible (to reduce the peak heat flux from bursts of previously confined EPs).

As discussed in section 5, simulations show resonances between EP motion and applied 3D fields are expected for typical DIII-D operating parameters. Future experiments will seek to understand the practical limitations of actually measuring the impact of these resonances and eventually exploiting them as a means to control localized regions of EP phase space.

Acknowledgments

References

[1] Spong D.A. 2011 *Phys. Plasmas* **18** 056109
[2] Garcia-Munoz M. *et al* 2013 *Nucl. Fusion* **53** 123008
[3] Garcia-Munoz M. *et al* 2013 *Plasma Phys. Control. Fusion* **55** 124014
[4] Van Zeeland M.A. *et al* 2014 *Plasma Phys. Control. Fusion* **56** 015009
[5] Shinohara K. *et al* 2011 *Nucl. Fusion* **51** 063028
[6] Heyn M.F., Ivanov I.B., Kasilov S.V., Kernbichler W., Loarte A., Nemov V.V. and Runov A.M. 2012 *Nucl. Fusion* **52** 054010
[7] Koskela T., Asunta O., Hirvijoki E., Kurki-Suonio T. and Akaslompolo S. 2012 *Plasma Phys. Control. Fusion* **54** 105008
[8] Tani K., Shinohara K., Oikawa T., Tsutsui H., Miyamoto S., Kusama Y. and Sugie T. 2012 *Nucl. Fusion* **52** 013012
[9] Asunta O., Akaslompolo S., Kurki-Suonio T., Koskela T., Sipilä A., Snicker A., Garcia-Minñoz M. and the ASDEX Upgrade Team 2012 *Nucl. Fusion* **52** 094014
[10] Snicker A., Hirvijoki E. and Kurki-Suonio T. 2013 *Nucl. Fusion* **53** 093028
[11] Fisher R.K., Pace D.C., Garc'a-Muñoz M., Heidbrink W.W., Muscatello C.M., Van Zeeland M.A. and Zhu Y.B. 2010 *Rev. Sci. Instrum.* **81** 10D307
[12] Pace D.C. *et al* 2010 *Rev. Sci. Instrum* **81** 10D305
[13] Chen X., Fisher R.K., Pace D.C., Garcia-Munoz M., Chavez J.A., Heidbrink W.W. and Van Zeeland M.A. 2012 *Rev. Sci. Instrum.* **83** 10D707
[14] Luo Y., Heidbrink W.W., Burrell K.H., Kaplan D.H. and Gohil P. 2007 *Rev. Sci. Instrum.* **78** 033505
[15] Ferraro N.M. and Jardin S.C. 2009 *J. Comput. Phys.* **228** 7742
[16] Ferraro N.M. 2012 *Phys. Plasmas* **19** 056105

[17] Ferraro N.M. *et al* 2012 *Proc. 24th IAEA Fusion Energy Conf.* (*San Diego, California, 8–13 October 2012*) TH/P4-21 www-naweb.iaea.org/napc/physics/FEC/FEC2012/papers/184_THP421.pdf

[18] Ferraro N.M., Evans T.E., Lao L.L., Moyer R.A., Nazikian R., Orlov D.M., Shafer M.W., Unterberg E.A., Wade M.R. and Wingen A. 2013 *Nucl. Fusion* **53** 073042

[19] Moyer R.A. *et al* 2012 *Nucl. Fusion* **52** 123019

[20] Stoschus H. *et al* 2012 *Nucl. Fusion* **52** 083002

[21] Chapman I.T. *et al* 2014 *Nucl. Fusion* **54** 083006

[22] Kramer G.J., Budny R.V., Bortolon A., Fredrickson E.D., Fu G.Y., Heidbrink W.W., Nazikian R., Valeo E. and Van Zeeland M.A. 2013 *Plasma Phys. Control. Fusion* **55** 025013

[23] Pankin A., McCune D., Andre R., Bateman G. and Kritz A. 2004 *Comput. Phys. Commun.* **159** 157

[24] Heidbrink W.W., Liu D., Luo Y., Ruskov E. and Geiger B. 2011 *Commun. Comput. Phys.* **10** 716

[25] Atomic Data and Analysis Structure (ADAS) compilation (http://adas.phys.strath.ac.uk)

[26] Chen X. *et al* 2014 *Rev. Sci. Instrum.* **85** 11E701

[27] Evans T.E. *et al* 2004 *Phys. Rev. Lett.* **92** 235003

[28] Evans T.E. *et al* 2008 *Nucl. Fusion* **48** 024002

[29] Lasnier C.J. *et al* 2014 *Rev. Sci. Instrum.* **85** 11D855

[30] Wingen A., Schmitz O., Evans T.E. and Spatschek K.H. 2014 *Phys. Plasmas* **21** 012509

[31] Schaffer M.J. 2008 *Nucl. Fusion* **48** 024004

[32] Kurki-Suonio T., Hirvijoki E., Sipil S., Gagliardi M., Akaslompolo S., Koskela T., Asunta O., Sarkimaki K. and Snicker A. 2014 ITER energetic particle confinement in the presence of ELM control coils and European TBMs *25th IAEA Int. Conf. on Fusion Energy* (*St Petersburg, Russia, 13–18 October 2014*) TH/P3-30

[33] Bortolon A. *et al* 2013 *Phys. Rev. Lett.* **110** 265008

[34] Mynick H.E. *et al* 1993 *Phys. Fluids* B **5** 1471

[35] Mynick H.E. and Pomphrey N. 1994 *Nucl. Fusion* **34** 1277

[36] Poli E., Garcia-Munõz M., Fahrbach H.-U., Günter S. and ASDEX Uptrade Team 2008 *Phys. Plasmas* **15** 032501

[37] Kramer G.J., Chen L., Fisher R.K., Heidbrink W.W., Nazikian R., Pace D.C. and Van Zeeland M.A. 2012 *Phys. Rev. Lett.* **109** 035003